ORIGINAL PAPER

A unique hierarchical composite with auricular-like MoS$_2$ nanosheets erected on graphene for enhanced lithium storage

Xiaowen Liu[1,2] · Gang Liu[1,2] · Changqiang Yu[1,2] · Lan Xie[1,2] · Yingjie Chen[1,2]

Abstract

Molybdenum disulfide (MoS$_2$) is a promising anode material in lithium-ion batteries (LIBs) due to its high specific capacity and typical two-dimensional layered structure. In this work, the MoS$_2$-graphene composite with unique hierarchical structure was successfully prepared by ethanolamine-assisted hydrothermal method. Raman spectroscopy showed that MoS$_2$ in the composite was a single or double layer. And the I_D/I_G value (1.13) of the composite indicated that it had some defects and disordered structure. X-ray photoelectron spectra illustrated that the majority of Mo and S elements existed in the composite in the form of Mo^{4+} and S^{2-}, and the Mo to S atomic ratio was 1:1.89. Scanning electron microscopy images showed that the majority of auricular-like MoS$_2$ nanosheets uniformly distributed upright on the graphene surface. Serving as anode material for LIBs, the composite exhibited a high reversible specific capacity, 1133 mAh g^{-1} (90.4% of the initial capacity) at 200 mA g^{-1} after 150 cycles. In addition, a specific capacity of 774 mAh g^{-1} was still achieved even at a high current density of 1000 mA g^{-1} after 600 cycles. The excellent electrochemical property of the composite was attributed to the combined action of unique hierarchical architecture, unstacked MoS$_2$ nanosheets, and highly conductive graphene. This work may offer a rational strategy for synthesizing transition mental sulfide-graphene composite with two-dimensional hierarchical structure as high-performance LIBs anodes.

Keywords MoS$_2$-graphene composite · Hierarchical structure · Hydrothermal method · Electrochemical property · Lithium-ion batteries

Introduction

With initial commercial application of lithium-ion batteries (LIBs) manufactured, it has captured the portable market in recent decades [1]. To cope with the rapid development of hybrid electric vehicles (HEVs) as well as plug-in hybrids (PHEVs), LIBs with higher energy density, lower cost, and better safety are still indispensable [1–3]. Graphite is the most common anode for commercial LIBs, due mainly to its low

✉ Xiaowen Liu
  lxwdr@csu.edu.cn

1 School of Minerals Processing and Bioengineering, Central South University, Changsha 410083, China

2 Key Laboratory for Mineral Materials and Application of Hunan Province, Central South University, Changsha 410083, China

working voltage, high reversibility, environmental protection, safety, and low cost [4]. Commercial graphite electrode, however, hardly meets the ever-growing demands on account of its unsatisfactory theoretical specific capacity (372 mAh g^{-1}). Other high theoretical capacity anode materials such as silicon (Si) (4200 mAh g^{-1}) and tin (994 mAh g^{-1}) have been considered as an alternative to the graphite anode [5, 6]. Nevertheless, the commercialization of these materials has been delayed resulting from its low intrinsic conductivity and large volume changes during cycling. Different approaches have been employed to stabilize the long-term cycling of Si-based and Sn-based anodes, including carbon coating, nano-crystallization, various structures (porous, core-shell, sandwich), and modification with other materials [7–11].

Molybdenum disulfide (MoS$_2$), a typical two-dimensional material, has recently attracted special attention as the next-generation high-performance LIB anodes by means of its high theoretical capacity (669 mAh g^{-1}), large layer spacing (0.62 nm), and low cost [12–15]. The unique structure of S-Mo-S atoms stacked together by weak van der Waals interactions can facilitate the intercalation and deintercalation of

lithium ions (Li$^+$) [12]. However, MoS$_2$ still suffered from the inherent low conductivity (2×10^{-4} S cm^{-1}), significant volume effects from the reaction mechanism, and poor utilization of the active substances, leading to the poor cycle stability and rate capability [13–15]. Various carbonaceous materials were compounded to address the above challenges, including carbon paper [16], carbon nanotubes [17], carbon fibers [18, 19], and graphene [20–32]. The incorporation of carbonaceous materials into MoS$_2$ contributed to improved electrical conductivity and reduced volume effect, which resulted in excellent cycle performance and rapid kinetic response of LIBs [17, 20]. Remarkably, graphene as a basement showed a great promise to anchor MoS$_2$ nanosheets owing to the fascinating structure, extraordinary electronic properties, and high mechanical strength [20, 21]. The significant progress has been made on the preparation and electrochemical performance of MoS$_2$-graphene (MoS$_2$-GR) composite as anodes for LIBs. Lei et al. adopted dopamine, dispersant in the reaction, and nitrogen source, to assist hydrothermal synthesis of MoS$_2$ nanosheets and nitrogen-doped graphene composite with a specific capacity of 1102 mAh g^{-1} at 100 mA g^{-1} current density after 100 cycles [21]. The mesoporous MoS$_2$/reduced graphene oxide composite was fabricated via a supercritical methanol, which displayed a specific capacity of 896 mAh g^{-1} at 50 mA g^{-1} after 50 cycles [22]. Zhao et al. prepared the core-shell MoS$_2$@graphene microspheres with a reversible capacity of 894 mAh g^{-1} at 100 mA g^{-1} after 1000 cycles [23]. In addition, stacking modes and tight coupling played a crucial role in utilization, charge transfer capability, and structural stability during cycling. Reasonable design and control of the growth coupling mode between MoS$_2$ and graphene were essential to further enhance the electrochemical lithium storage ability of the composite.

In this work, we adopted a facile one-pot hydrothermal route to prepare a unique hierarchical structure of MoS$_2$-GR composite by ethanolamine (ETA)-assisted method. And a possible growth mechanism for the MoS$_2$-GR composite with unique hierarchical structure was proposed. The unique vertically aligned architecture and the intimate contact of MoS$_2$ nanosheets with graphene having high conductivity and large specific surface area could effectively provide abundant reactive sites, reduce volume expansion, and impart excellent electron transport rate. As the result, the composite exhibited a high reversible specific capacity, excellent cycle stability, and good rate capability.

Experimental

Materials

Natural flake graphite powder (size ≤ 48 μm, purity $\geq$ 99.99%) was purchased from Shimen, Hunan, China.

Sodium molybdate dihydrate (Na$_2$MoO$_4 \cdot$2H$_2$O, 99.99%), thioacetamide (C$_2$H$_5$NS, 99.0%), ETA (C$_2$H$_7$NO, 99.5%), glacial acetic acid (C$_2$H$_4$O$_2$, 99.0%), polyvinylidene fluoride (PVDF), and acetylene black were purchased from Aladdin Reagent Co. Ltd. (Shanghai, China). N-methyl-2-pyrrolidinone (NMP, 99.5%), potassium permanganate (KMnO$_4$, 99.5%), sodium nitrate (NaNO$_3$, 99%), and hydrogen peroxide (H$_2$O$_2$, 30%) were obtained from Sinopharm Chemical Reagent Co. Ltd. (Shanghai, China). Concentrated sulfuric acid (H$_2$SO$_4$, 98%) and concentrated hydrochloric acid (HCl, 38%) were purchased from Huihong Co. Ltd. (Hunan, China). Electrolyte purchased from New Zealand Bang Technology Co. Ltd. (Shenzhen, China). All chemical reagents were of analytical grade without further purification. The deionized water was used during the experiment.

Synthesis of MoS$_2$-GR composite

GO was made from natural graphite by a modified Hummers' method, as we reported previously [33]. In a typical process, as-prepared 48 mg GO powder was added to 50 mL deionized water to form a homogeneous suspension after ultrasonicated for 2 h. The suspension was then mixed with ETA (2 mL) and C$_2$H$_4$O$_2$ (5 mL), and kept stirring for 10 h at room temperature. Afterwards, Na$_2$MoO$_4 \cdot$2H$_2$O (0.363 g) and C$_2$H$_5$NS (0.375 g) were sequentially added into the above mixture and stirred for 2 h. Subsequently, the mixed solution was transferred into a 100-mL Teflon-lined stainless steel autoclave and heated to 200 °C for 24 h. After cooling naturally, the black precipitates were collected by centrifugation and washed three times with deionized water and ethanol, respectively, followed by freeze drying for 12 h. Finally, the MoS$_2$-GR composite was obtained by annealing of as-prepared black precipitates at 800 °C for 2 h in argon atmosphere.

Characterization

X-ray diffraction (XRD) patterns were obtained from a DX-2700 diffractometer (Haoyuan, China) with Cu Kα radiation ($\lambda = 1.54056$ Å), operating at 40 kV and 40 mA in the 2θ range from 3° to 80°. ZEN 3600 (Malvern, UK) was employed to characterize the surface zeta potential of the samples. Fourier transform infrared spectra (FT-IR) were recorded on a Nexuc670 spectrophotometer (Nicolet, USA) with a wavelength range of 400–4000 cm^{-1}. Raman spectra were carried out on an inVia spectrometer (Renishaw, UK) with laser excitation at 532 nm, and the spectral recording range was 100–2000 cm^{-1}. The nitrogen adsorption-desorption isotherms were recorded by an N$_2$ adsorption device (Micromeritics 2020, USA). X-ray photoelectron spectra (XPS) were performed on an ESCALAB 250Xi spectrometer (Thermo Fisher, USA) with an Al Kα (1486.6 eV). The field-emission scanning electron microscope (FE-SEM) images
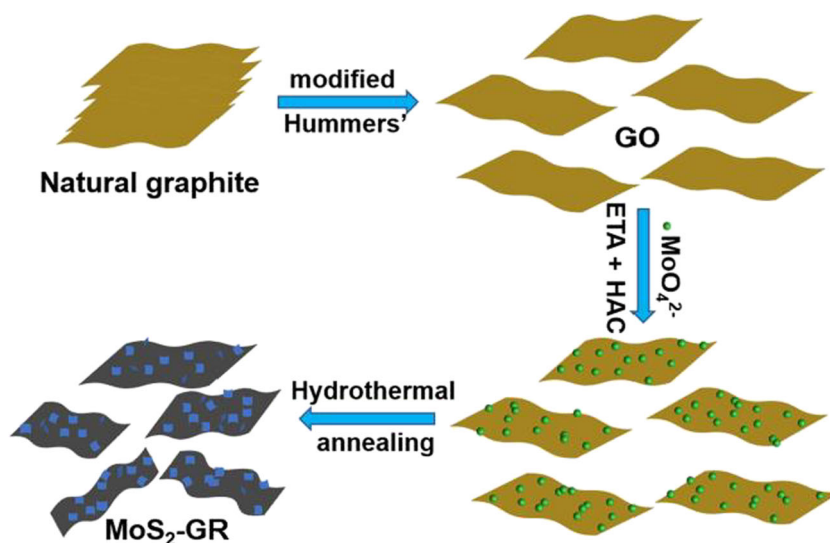
were observed using a MIRA3 (TESCAN, Czech) manipulating at 20 kV. The transmission electron microscope (TEM) images were obtained by a Titan G2 60-300 (FEI, USA) with an accelerating voltage of 200 kV.

Electrochemical measurements

The slurry of active materials (MoS_2-GR composite, bare MoS_2) was prepared by mixing the active material, PVDF binder, and acetylene black in a mass ratio of 7:2:1 blended in NMP. The mixed slurry was uniformly coated on a copper foil with a thickness of 10 μm, and vacuum dried in an oven (DZF-6050, Jinghong, China) at 60 °C for 12 h. Then, it was stamped into a circular piece (diameter of 14 mm) with mass loading of 0.8–0.9 mg cm^{-2} basing on the total weight of MoS_2 and graphene. CR2032-type coin cells were assembled in glove box (ZK-82B, MIKROUNA, China) filled with high purity argon with both moisture and oxygen levels below 0.1 ppm. Metallic lithium and Celgard 2400 polypropylene film were used as a counter electrode and separator during assembling, respectively. 1 M $LiPF_6$ in a mixture of ethylene carbonate (EC)/dimethyl carbonate (DMC) (1:1 by volume) was used as the electrolyte. The cycle stability of the cells was carried out on the battery test system (BTS80, Xinwei, China) at different current densities with a voltage platform range of 0.01–3 V. Cyclic voltammetry (CV) was performed on an electrochemical workstation (INTERFACE 1010, Gamry, USA) at a scan rate of 0.2 mV s^{-1} in a voltage range of 0.01–3 V. The frequency range of electrochemical impedance spectra (EIS) was 0.01–10^6 Hz.

Results and discussion

MoS_2-GR composite has been synthesized by hydrothermal method [24–26], electrosynthesis [20], chemical vapor deposition [34], and spray pyrolysis [23, 29]. Scheme 1 illustrated the synthesis strategy of hierarchical MoS_2-GR composite via
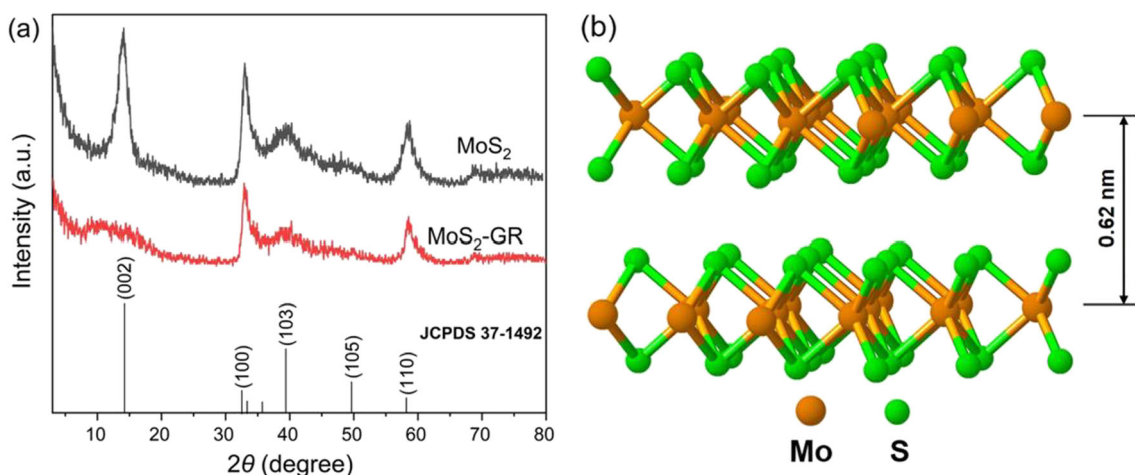
Fig. 1 **a** XRD patterns of MoS_2 and MoS_2-GR composite. **b** A schematic diagram of crystal structure of 2H-MoS_2
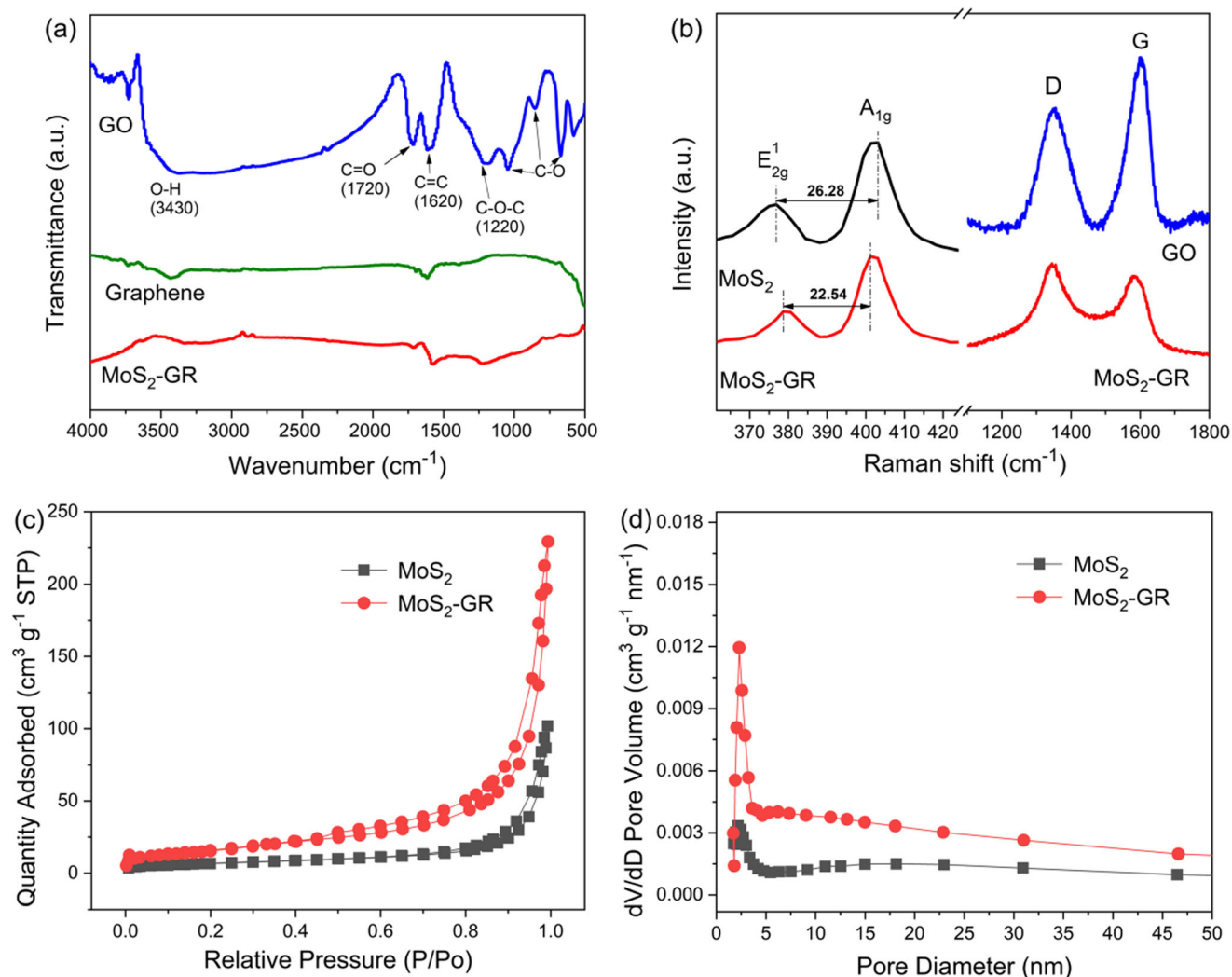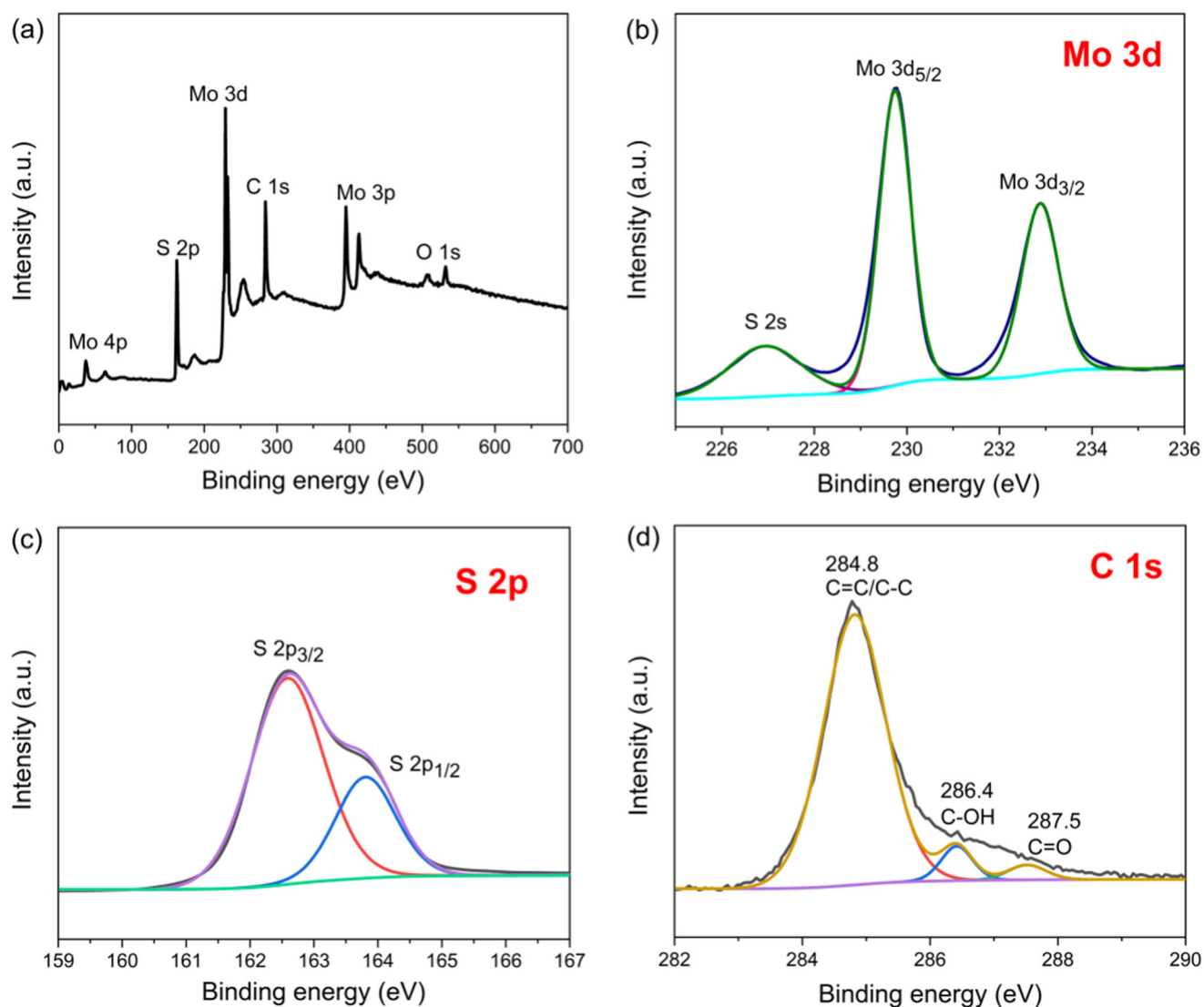
Fig. 2 **a** FT-IR spectra of GO, graphene, and MoS_2-GR composite. **b** Raman spectra of GO, MoS_2, and MoS_2-GR composite. **c** Nitrogen adsorption-desorption isotherms and (**d**) pore-size distributions of MoS_2 and MoS_2-GR composite

a facile hydrothermal method. In this work, we adopted ETA and glacial acetic acid to assist in the synthesis of the composite. The surface of GO would be positively charged (Fig. S1), resulting in good electrostatic adsorption between GO and Mo sources. ETA could be also used as a linker to induce and modulate the uniform growth of MoS_2 nanosheets on the graphene surface in the hydrothermal process. The introduction of $C_2H_4O_2$ was employed to adjust the pH of the solution and accelerate the hydrolysis reaction of the S source. Graphene acted as a substrate for nucleation and growth of MoS_2 in hydrothermal reactions. As expected, MoS_2 nanosheets uniformly distributed upright on the graphene surface. One possible reason was that the base face of graphene has a heterogeneous charge with the edge face of MoS_2, and the same charge as the base face of MoS_2 at pH 2.5, which is consistent with previous reports [35, 36]. From the kinetic theory, when the Mo source was vulcanized, MoS_2 would tend to grow vertically rather than horizontally on the

substrate because the strain energy caused by the two-dimensional growth could be released by the expansion in the vertical direction [37]. Additionally, the sulfur diffusion along the layers through van der Waals gaps was much faster than diffusion across the layers, resulting in the faster growth in the vertical orientation [37–39].

As shown in XRD patterns (Fig. 1a), 2H-MoS_2 (JCPDS 37-1492) was successfully prepared after the hydrothermal process and subsequent annealing. The dominant (002) diffraction peak of pure MoS_2 illustrated a well-stacked structure in the c-axis direction, and the interplanar spacing was calculated as 0.618 nm (Fig. 1b). On the contrary, (002) diffraction peak of MoS_2 in the composite was broadened and weakened, suggesting it had the structure of single layer or few layers [27–30]. The characteristic peak ($\approx 26°$) of graphene was not shown in the composite due to the relatively small amount of graphene. Additionally, it may be attributed to the

Fig. 3 XPS spectra of MoS$_2$-GR composite. **a** Survey spectrum, **b** Mo 3d spectrum, **c** S 2p spectrum, and **d** C 1s spectrum

layered MoS$_2$ anchored onto the graphene surface and inhibited the accumulation of graphene sheets [26].

The infrared spectra of GO, graphene, and MoS$_2$-GR composite were characterized in Fig. 2a. There was a strong and broad absorption peak at 3430 cm^{-1} in the GO (O–H stretching vibration). The additional characteristic peaks of GO corresponded to C=O, C=C, C–O–C, and C–O bonds emerged at 1720 cm^{-1} [40], 1620 cm^{-1} [26], 1220 cm^{-1} [41], and 1150 cm^{-1} [26], respectively. The absence of the peak of oxygen-containing functional groups in the graphene and MoS$_2$-GR curves confirmed that GO was almost completely reduced. Raman spectra of GO, MoS$_2$, and MoS$_2$-GR composite were exhibited in Fig. 2b. The E1 2g mode was bound up with the intralayer displacement of Mo and S atoms, while A$_{1g}$ mode was related to the interlaminar symmetric displacement of S atoms along the c-axis [19, 42]. In pure MoS$_2$, the E1 2g and A$_{1g}$ peaks of MoS$_2$ appeared at

376.90 and 403.18 cm^{-1} with a peak separation of 26.28 cm^{-1} (more than 24.2 cm^{-1} of four-layer MoS$_2$ nanosheets) [43, 44]. In the composite, there was a peak separation of 22.54 cm^{-1} between the E1 2g and A$_{1g}$ peaks, which meant single-layer or two-layer MoS$_2$ nanosheet [44]. Compared with the pristine MoS$_2$, the E1 2g and A$_{1g}$ peaks of MoS$_2$-GR were weaker and broader by means of phonon limitation, the typical for layered structure [27]. The D peak meant the defects and disorder in the hexagonal pattern layer, and the G peak was implied to the vibration of sp^2 carbon atoms in the two-dimensional hexagonal lattice [24]. The G peaks of GO and the composite were located at 1598 and 1582 cm^{-1}, respectively, demonstrating the reduction of GO to GR [45, 46]. The I_D/I_G value of GO was 0.79, but that of the composite was 1.13. This increase in the I_D/I_G value illustrated a decrease in the average size of the sp^2 domains upon reduction of GO, further confirming the existence of GR in the composite [24,

Fig. 4 SEM images of MoS$_2$ (**a**, **b**) and MoS$_2$-GR composite (**c**, **d**). **e** SEM element mapping images of MoS$_2$-GR composite
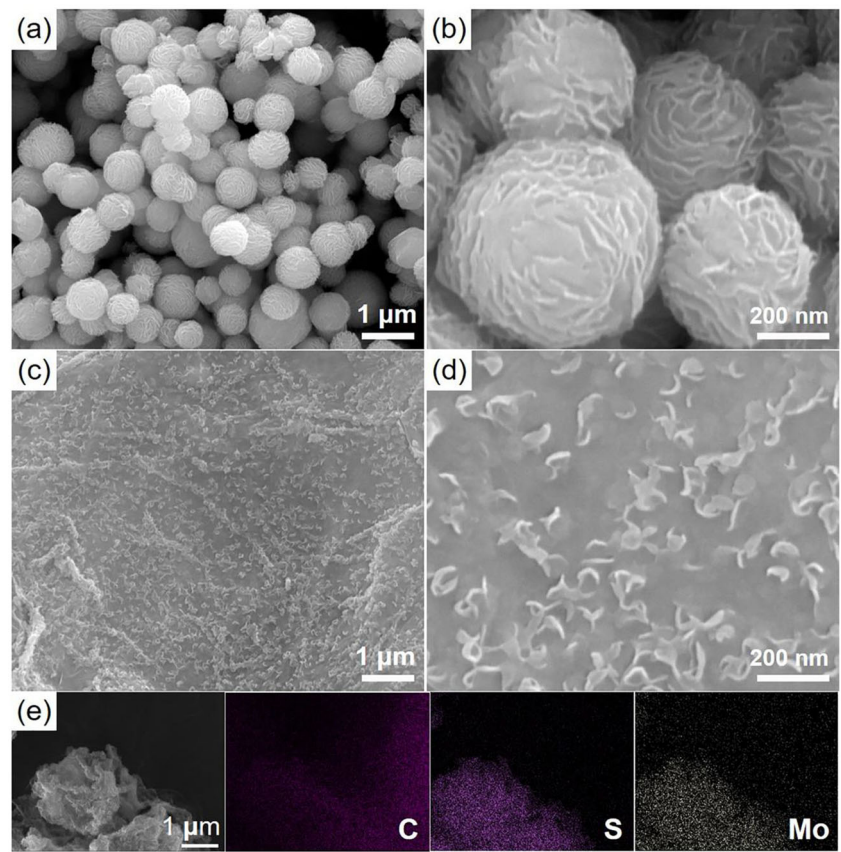
Fig. 5 TEM (**a**), HRTEM (**b**, **c**), and SAED (**d**) images of MoS$_2$-GR composite
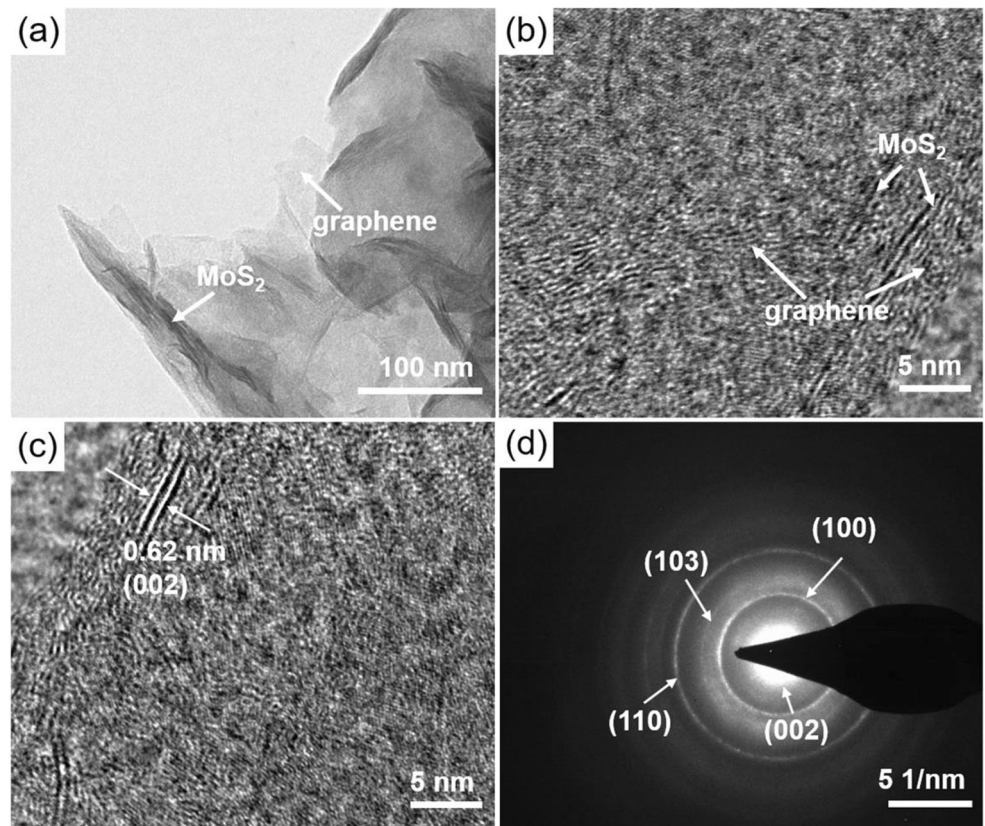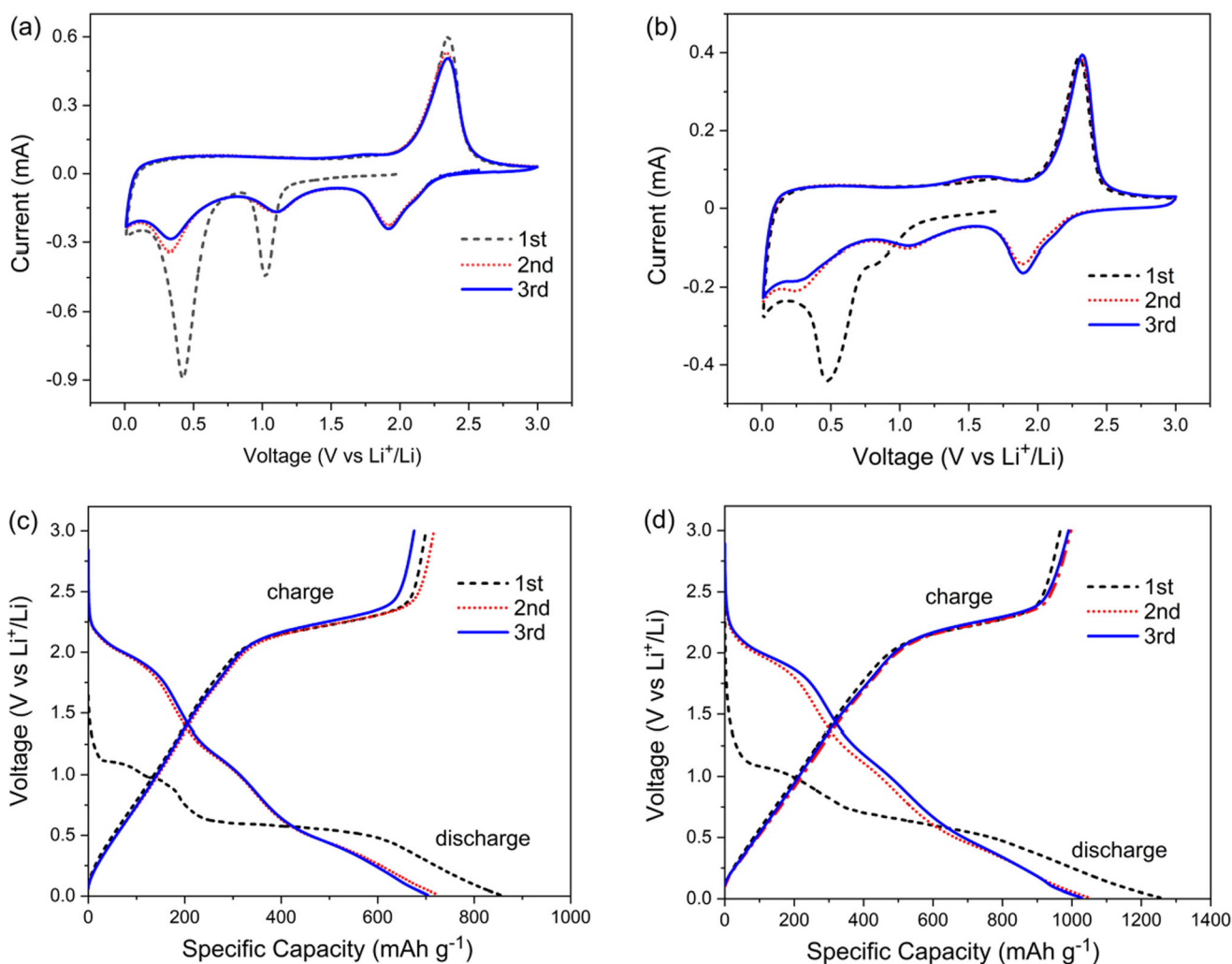
Fig. 6 CV curves of the first three cycles for MoS_2 (**a**) and MoS_2-GR composite (**b**) at a scan rate of 0.2 mV s^{-1}. The first three galvanostatic charge/discharge curves of MoS_2 (**c**) and MoS_2-GR composite (**d**) at 200 mA g^{-1}

46]. Additionally, the I_D/I_G value (1.13) of the composite indicated that it had some defects and disordered structure. These defects might help forming stable interface on graphene during electrochemical reaction. The stable interface could protect the electrode well, while allowing rapid lithiation/delithiation [47].

The specific surface area and pore-size distribution of MoS_2 and MoS_2-GR composite were obtained by the nitrogen adsorption-desorption test. Figure 2 c showed that two samples exhibited typical IV isotherms with hysteresis loops ($P/P_0 > 0.45$), indicating the existence of mesoporous structure [48]. The Brunauer-Emmett-Teller (BET) surface area of the composite (57.85 m^2 g^{-1}) was 2.4 times than that of pure MoS_2 (24.55 m^2 g^{-1}). This should be attributed to the incorporation of graphene could effectively inhibit the accumulation or growth of MoS_2 nanosheets along the c-axis, which agreed with the analysis of XRD patterns and Raman spectra. Large specific surface area could ensure rich reactive sites, resulting in a high material utilization. The pore-size

distributions of two samples were similar, mainly showing mesopores (Fig. 2d). As shown in Table S1, the pour volume of MoS_2-GR composite was 0.36 cm^3 g^{-1} (larger than 0.16 cm^3 g^{-1} of pure MoS_2). The rich mesopores and large pore volume contributed to the migration of Li$^+$ and cycle stability [30].

XPS were performed to analyze the chemical composition and elemental valence of the composite. The full spectrum of MoS_2-GR composite (Fig. 3a) suggested that it was consisted of Mo, S, C, and a very small amount of O. In the Mo 3d spectrum (Fig. 3b), two bands located at 232.8 and 229.7 eV were indicative of doublet the Mo 3d$_{3/2}$ and Mo 3d$_{5/2}$, typical for Mo^{4+} in MoS_2 [20]. Another peak at 226.8 eV represented the S 2s component. In Fig. 3c, the binging energy of S 2p$_{1/2}$ and S 2p$_{3/2}$ peaks located at 163.7 and 162.5 eV, respectively, which could be indexed to S^{2-} in MoS_2 [49]. As shown in Fig. 3d, the dominant peak at 284.8 eV was related to C=C/C–C bonds [42]. Two other peaks with low intensity at 286.4 and 287.5 eV matched respectively the C–OH and C=O bonds,
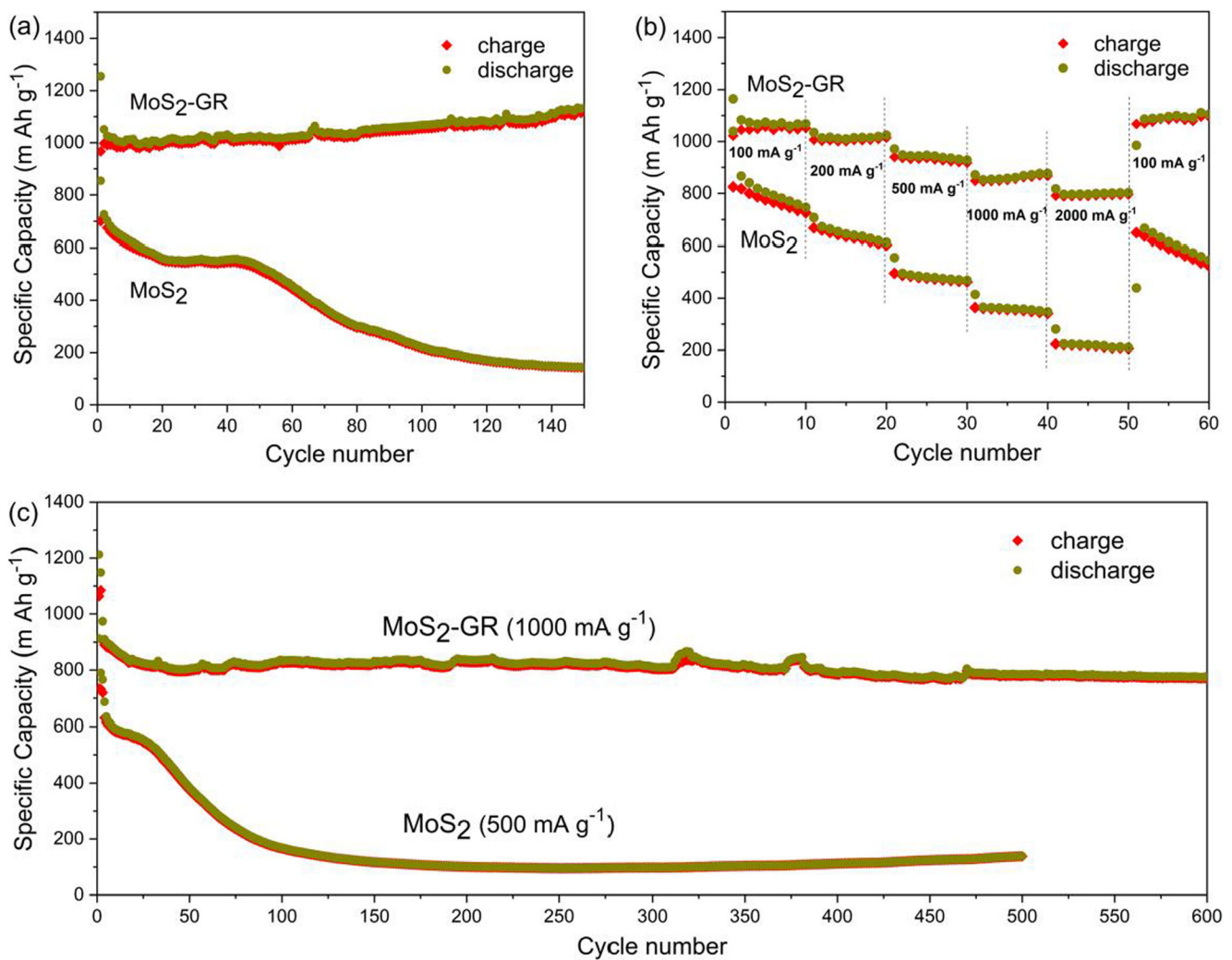
Fig. 7 **a** Cycling performance of MoS$_2$ and MoS$_2$-GR composite at 200 mA g^{-1}. **b** Rate capability of MoS$_2$ and MoS$_2$-GR composite at the current densities ranging from 100 to 2000 mA g^{-1}. **c** Cycling performance of MoS$_2$ at 500 mA g^{-1} and MoS$_2$-GR composite at 1000 mA g^{-1}

signifying that most of GO was reduced to graphene [22]. In addition, the atomic ratio of Mo to S was 1:1.89.

The SEM images (Fig. 4a, b) exhibited that MoS$_2$ nanoflower-like spherical particle (300–800 nm) was self-assembled from nanosheets with the thickness of 8–15 nm and the length of 200–300 nm. However, MoS$_2$-GR composite exhibited a particularly hierarchical structure in Fig. 4c. More detailed observation in Fig. 4d showed that auricular-like MoS$_2$ nanosheets were erected and evenly arrange on the graphene surface. The thickness and length of the MoS$_2$ nanosheets were 5–10 and 50–100 nm, respectively. The auricular-like and highly dispersed MoS$_2$ nanosheets would exist abundant reactive sites generated by a large specific surface area, resulting in a significant increase in the reversible specific capacity. The ultrasmall size could shorten the diffusion distance of Li$^+$ and accelerate the active material/electrolyte interface reaction. The SEM element mapping images (Fig. 4e) also confirmed that C, S, and Mo elements were

homogeneously distributed in the MoS$_2$-GR composite. In addition, the composite had a strong skeleton, maintaining sufficiently internal space to prevent effectively reaggregation of the active substance upon repeated Li$^+$ insertion and extraction. The TEM images (Fig. 5a) displayed that graphene was also observed as a carrier for MoS$_2$ growth. As shown in Fig. 5b, c, MoS$_2$-GR composite contained highly dispersed MoS$_2$ with single layer or a few layers. Basing on the high-resolution TEM (HRTEM) picture, the interlayer distance of the (002) crystal plane was measured to be 0.62 nm. These diffraction rings in the selected area electron diffraction (SAED) images (Fig. 5d) were well-indexed to the (002), (100), (103), and (110) planes of 2H-MoS$_2$.

The electrochemical Li$^+$ storage mechanism of two electrodes was discussed by CV measurements with a scan rate of 0.2 mV s^{-1} (Fig. 6a, b). Two reduction peaks located at ≈ 0.96 and 0.48 V could be found for the first cathode scan. The broad peak at ≈ 0.96 V was associated with the Li$^+$
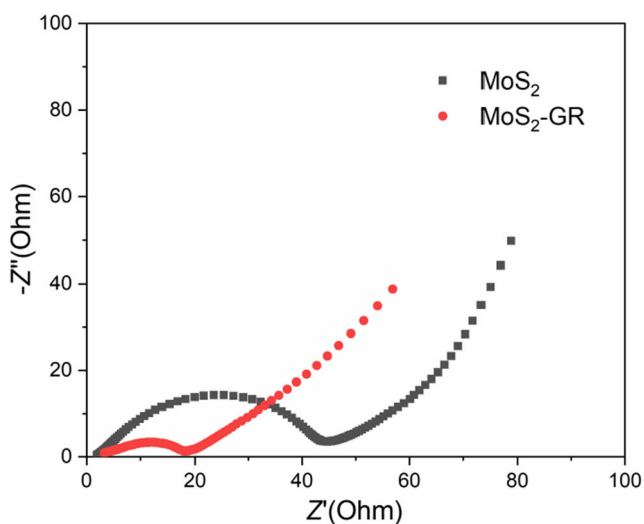
Fig. 8 SEM images of MoS₂ electrode (**a**, **b**) and MoS₂-GR composite (**c**, **d**) electrode after 50 cycles at 200 mA g^{-1}
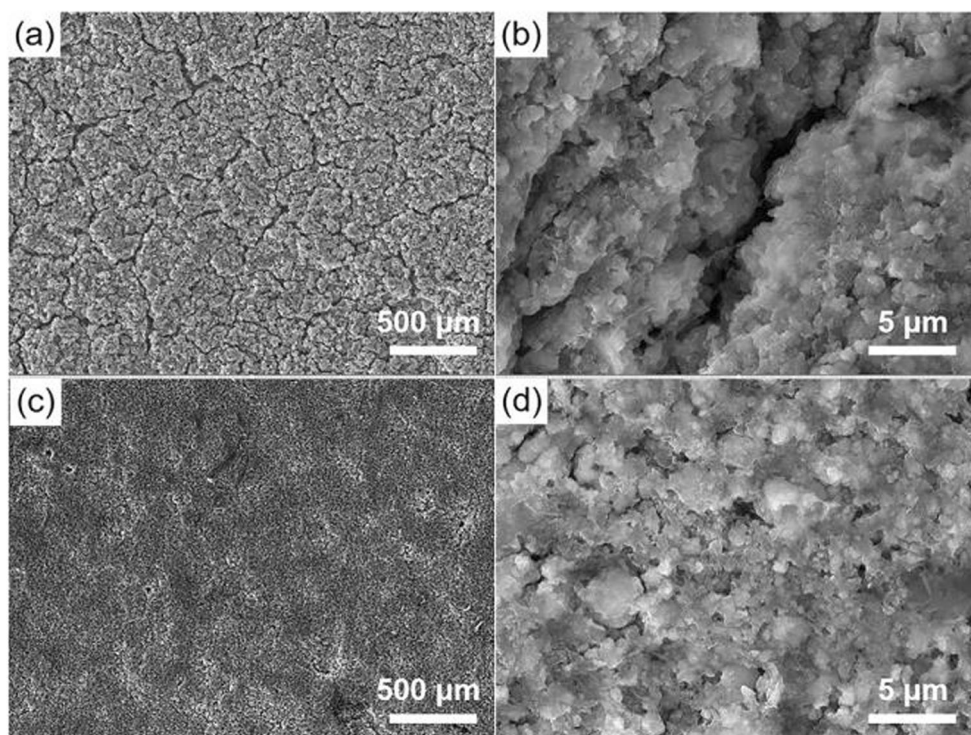
intercalation into the MoS₂ layers of 2H-MoS₂ to form the 1T structure of Li_xMoS_2 ($MoS_2 + xLi^+ + xe^- \rightarrow Li_xMoS_2$) [15, 21]. The dominant peak at 0.48 V corresponded to the transition of Li_xMoS_2 to metallic Mo and Li_2S ($Li_xMoS_2 + (4 - x)Li^+ + (4 - x)e^- \rightarrow Mo + 2Li_2S$) [32]. In the subsequent anode scan process, two anodic peaks located at 1.54 and 2.31 V, respectively, were ascribed to the partial oxidation of Mo to Mo^{4+} and the delithiation of Li_2S to S ($Li_2S \rightarrow 2Li^+ + S + 2e^-$) [15, 32]. It should be mentioned that two cathodic peaks at ≈ 0.96 and 0.48 V disappeared in the later discharge

curves, suggesting the irreversible conversion of 2H-MoS₂ [49]. Instead, the strong reduction peak at 1.89 V was ascribed to S-lithiation to form Li_2S ($2Li^+ + S + 2e^- \rightarrow Li_2S$), and the other two weak peaks (1.05, 0.25 V) were attributed to Li^+ stored around Mo atoms and the lattice defects [31]. The MoS₂-GR electrode had a superior cycle stability during scanning owing to CV plots with good overlap in the subsequent reaction process. For MoS₂, the CV curves was resembled to that of the composite, illustrating that the addition of graphene had no significant effect on the reaction mechanism of electrochemical lithium storage. However, graphene could greatly improve the cycle stability of the composite. Figure 6 c and b revealed the galvanostatic charge-discharge curves of the first three turns of the two electrodes at 200 mA g^{-1}. The voltage platform in the charge-discharge curves coincided with CV measurements. Apart from the large consumption of the initial cycle, the specific capacity of the MoS₂-GR electrode did not decrease visibly at the latter two cycles. By comparison, the MoS₂ electrode performed a dramatic specific capacity decay during cycling.

The above conclusions were further certificated by the cycle life profiles of the two electrodes (Fig. 7a). The specific discharge capacity and retention of the MoS₂-GR electrode were 1133 mAh g^{-1} and 90.4% at 200 mA g^{-1} after 150 cycles, respectively. In contrast, after 150 cycles, the pure MoS₂ electrode had a capacity retention of 16.9%, and the discharge specific capacity dropped to 144 mAh g^{-1}. The initial charge-discharge specific capacities of the two electrodes were 967/1254 and 700/854 mAh g^{-1}, respectively,

Fig. 9 Nyquist plots of MoS₂ and MoS₂-GR composite electrodes after 150 cycles
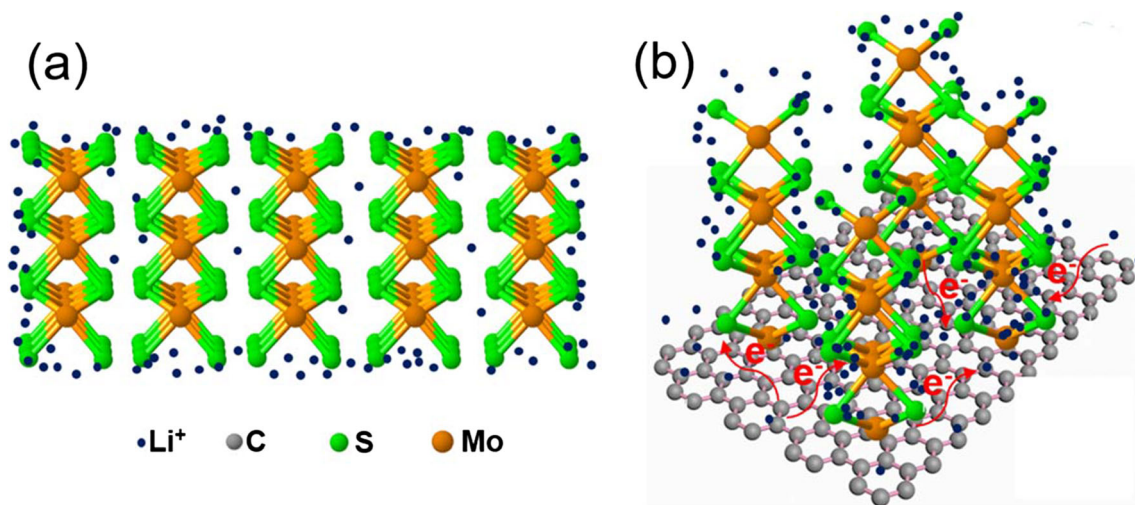
Fig. 10 Schematic illustration of paths of Li$^+$ migration of the MoS$_2$ electrode (**a**) and MoS$_2$-GR composite electrode (**b**)

corresponding to the coulombic efficiencies of 77.1 and 82.0% (Fig. S4). The rapid decay of capacity of the first loop might be ascribe to the formation of solid electrolyte interphase (SEI) film, Li$^+$ storage in the lattice defects, and the decomposition of electrolyte [18, 21]. The excellent cycling stability and high reversible specific capacity of the composite were also manifested in the rate capability. Figure 7 b displayed that the 10th-cycle corresponding discharge capacities of the MoS$_2$-GR were 1068, 1024, 924, 876, and 803 mAh g^{-1} at current densities of 100, 200, 500, 1000, and 2000 mA g^{-1}, respectively. The MoS$_2$ electrode delivered the10th-cycle delithiation capacities of 746, 613, 468, 348, and 210 mAh g^{-1}, respectively. When the current density returned to 100 mA g^{-1}, the discharge capacity of the MoS$_2$-GR electrode could be restored to 1104 mAh g^{-1}. Rapid charge-discharge recovery was a vital parameter in evaluating the performance of LIBs. As shown in Fig. 7c, the discharge capacity of the MoS$_2$-GR electrode of 774 mAh g^{-1} (63.8% of the initial capacity) could still be achieved even at a high current density of 1000 mA g^{-1} after 600 cycles. Nevertheless, the MoS$_2$ electrode displayed an unsatisfied

capacity (138 mAh g^{-1} at 500 mA g^{-1} after 500 cycles). Figure 8 compared the SEM images of the two electrodes after 50 cycles at 200 mA g^{-1}. Obviously, there are wide cracks on the surface of the MoS$_2$ electrode, and the volume changed greatly. The composite electrode still maintained the structural stability better, further illustrating the excellent cycle performance.

EIS could be applied for the evaluation of electrochemical kinetics. The Nyquist plots of MoS$_2$ and MoS$_2$-GR electrodes after 150 cycles at 200 mA g^{-1} were plotted in Fig. 9. Obviously, two Nyquist plots were composed of two semicircles at high frequency and a diagonal line at low frequency. The semicircle of the high frequency region represented the charge transfer process between the electrode material and the electrolyte, and the low-frequency oblique line corresponded to the Li$^+$ diffusion process [28]. Obviously, the composite electrode with a smaller semicircular diameter was endowed with the lower charge transfer resistance than the MoS$_2$ electrode [48].

As consequence, MoS$_2$-GR composite electrode performed better in terms of cycle stability, reversible capacity,

Table 1 LIBs performance summary of MoS$_2$-based composites

Sample	Initial CE (%)	Capacity/current	References
MoS$_2$-GR	77.1	1133 mA h g^{-1} at 0.2 A g^{-1} (150th cycle)	This work
		774 mA h g^{-1} at 1 A g^{-1} (600th cycle)	
MoS$_2$/N-graphene	62.3	1102 mA h g^{-1} at 0.1 A g^{-1} (100th cycle)	[21]
MoS$_2$-graphene	68.3	573 mA h g^{-1} at 0.1 A g^{-1} (50th cycle)	[25]
MoS$_2$-graphene	77.2	1077 mA h g^{-1} at 0.1 A g^{-1} (150th cycle)	[28]
		907 mA h g^{-1} at 1 A g^{-1} (400th cycle)	
MoS$_2$-graphene	73.8	970 mA h g^{-1} at 0.1 A g^{-1} (80th cycle)	[32]
MoS$_2$/N-C	72.8	904 mA h g^{-1} at 0.2 A g^{-1} (100th cycle)	[48]
		686 mA h g^{-1} at 1 A g^{-1} (400th cycle)	
C@MoS$_2$ nanotube sponges	86	740 mA h g^{-1} at 0.1 A g^{-1} (100th cycle)	[49]
		302 mA h g^{-1} at 0.8 A g^{-1}	

and rate capability in comparison to pure MoS_2 electrode. Figure 10 illustrated the paths of Li^+ migration of the MoS_2 electrode (a) and MoS_2-GR composite electrode (b). The ultrathin MoS_2 nanosheets were evenly distributed and strongly coupled on the graphene surface, which might buffer the mechanical stress induced by volume expansion of MoS_2 during repeated Li^+ insertion and extraction. The composite with unique geometry and large specific surface area would expose numerous active sites, increasing the reversible capacity of the electrode. Additionally, graphene could provide a high-performance electron transport network to accelerate the transport of Li^+.

Conclusions

In summary, MoS_2-GR composite with hierarchical architecture was successfully prepared by a facile one-pot hydrothermal method. When assembled into coin cells, the composite electrode exhibited a better reversible specific capacity, higher capacity retention, and longer cycle life than previously reports (Table 1). Excellent cycle performance was attributed to the abundant electrochemically active sites generated from MoS_2 nanosheets erected on graphene substrates. Furthermore, nanoscale materials could increase the area in contact with the electrolyte and shorten the distance of Li^+ diffusion. The unique geometry of nanocomposite could be considered as one of the most promising candidates for LIBs anode materials.

References

1. Dunn B, Kamath H, Tarascon JM (2011) Electrical energy storage for the grid: a battery of choices. Science 334(6058):928–935
2. Goodenough JB, Kim Y (2010) Challenges for rechargeable Li batteries. Chem Mater 22(3):587–603
3. Placke T, Kloepsch R, Dühnen S, Winter M (2017) Lithium ion, lithium metal, and alternative rechargeable battery technologies: the odyssey for high energy density. J Solid State Electrochem 21(7):1939–1964
4. Billaud J, Bouville F, Magrini T, Villevieille C, Studart AR (2016) Magnetically aligned graphite electrodes for high-rate performance Li-ion batteries. Nat Energy 1(8). https://doi.org/10.1038/nenergy.2016.97
5. Liu L, Lyu J, Li T, Zhao T (2016) Well-constructed silicon-based materials as high-performance lithium-ion battery anodes. Nanoscale 8(2):701–722
6. Guo J, Yang Z, Archer LA (2013) Aerosol assisted synthesis of hierarchical tin-carbon composites and their application as lithium battery anode materials. J Mater Chem A 1(31):8710–8715
7. Xu Y, Zhu Y, Liu Y, Wang C (2013) Electrochemical performance of porous carbon/tin composite anodes for sodium-ion and lithium-ion batteries. Adv Energy Mater 3(1):128–133
8. Zhuang X, Zhang Y, He L, Zhu Y, Tian Q, Guo X, Chen J, Li L, Wang Q, Song G, Yan X (2017) Scalable synthesis of nano-Si embedded in porous C and its enhanced performance as anode of Li-ion batteries. Electrochim Acta 249:166–172
9. Sasidharachari K, Na B-K, Woo S-G, Yoon S, Cho KY (2016) Facile conductive surface modification of Si nanoparticle with nitrogen-doped carbon layers for lithium-ion batteries. J Solid State Electrochem 20(10):2873–2878
10. Hong YJ, Kang YC (2015) One-pot synthesis of core-shell-structured tin oxide-carbon composite powders by spray pyrolysis for use as anode materials in Li-ion batteries. Carbon 88:262–269
11. Cui LF, Yang Y, Hsu CM, Cui Y (2009) Carbon-silicon core-shell nanowires as high capacity electrode for lithium ion batteries. Nano Lett 9(9):3370–3374
12. Xiao J, Choi D, Cosimbescu L, Koech P, Liu J, Lemmon JP (2010) Exfoliated MoS₂ nanocomposite as an anode material for lithium ion batteries. Chem Mater 22(16):4522–4524
13. Li X, Zai J, Xiang S, Liu Y, He X, Xu Z, Wang K, Ma Z, Qian X (2016) Regeneration of metal sulfides in the delithiation process: the key to cyclic stability. Adv Energy Mater 6(19):1601056
14. Stephenson T, Li Z, Olsen B, Mitlin D (2014) Lithium ion battery applications of molybdenum disulfide (MoS₂) nanocomposites. Energy Environ Sci 7(1):209–231
15. Wang G, Zhang J, Yang S, Wang F, Zhuang X, Müllen K, Feng X (2018) Vertically aligned MoS₂ nanosheets patterned on electrochemically exfoliated graphene for high-performance lithium and sodium storage. Adv Energy Mater 8(8):1702254
16. Xie X, Makaryan T, Zhao M, Van Aken KL, Gogotsi Y, Wang G (2016) MoS₂ nanosheets vertically aligned on carbon paper: a free-standing electrode for highly reversible sodium-ion batteries. Adv Energy Mater 6(5):1502161
17. Lu C, W-w L, Li H, Tay BK (2014) A binder-free CNT network-MoS₂ composite as a high performance anode material in lithium ion batteries. Chem Commun 50(25):3338–3334
18. Wang C, Wan W, Huang Y, Chen J, Zhou HH, Zhang XX (2014) Hierarchical MoS₂ nanosheet/active carbon fiber cloth as a binder-free and free-standing anode for lithium-ion batteries. Nanoscale 6(10):5351–5358
19. Zhu C, Mu X, van Aken PA, Yu Y, Maier J (2014) Single-layered ultrasmall nanoplates of MoS₂ embedded in carbon nanofibers with excellent electrochemical performance for lithium and sodium storage. Angew Chem Int Ed 53(8):2152–2156
20. Ge Y, Wang C, Zhao Y, Liu Y, Chao Y, Zheng T, Wallace GG (2018) An electrosynthesized 3D porous molybdenum sulfide/graphene film with enhanced electrochemical performance for lithium storage. Small 14(9):1703096
21. Lei Z, Xu L, Jiao Y, Du A, Zhang Y, Zhang H (2018) Strong coupling of MoS₂ nanosheets and nitrogen-doped graphene for high-performance pseudocapacitance lithium storage. Small 14(25):1704410
22. Choi M, Koppala SK, Yoon D, Hwang J, Kim SM, Kim J (2016) A route to synthesis molybdenum disulfide-reduced graphene oxide (MoS₂-RGO) composites using supercritical methanol and their enhanced electrochemical performance for Li-ion batteries. J Power Sources 309:202–211
23. Xue H, Wang J, Wang S, Muhammad S, Feng C, Wu Q, Li H, Shi D, Jiao Q, Zhao Y (2018) Core-shell MoS₂@graphene composite microspheres as stable anodes for Li-ion batteries. New J Chem 42:15340–15345
24. Wang Y, Zhen M, Liu H, Wang C (2018) Interlayer-expanded MoS₂/graphene composites as anode materials for high-performance lithium-ion batteries. J Solid State Electrochem 22(10):3069–3076

25. Zhao B, Wang Z, Gao Y, Chen L, Lu M, Jiao Z, Jiang Y, Ding Y, Cheng L (2016) Hydrothermal synthesis of layer-controlled MoS_2/graphene composite aerogels for lithium-ion battery anode materials. Appl Surf Sci 390:209–215

26. Liu Y, Zhao Y, Jiao L, Chen J (2014) A graphene-like MoS_2/graphene nanocomposite as a high-performance anode for lithium ion batteries. J Mater Chem A 2(32):13109–13115

27. Matte HS, Gomathi A, Manna AK, Late DJ, Datta R, Pati SK, Rao CN (2010) MoS_2 and WS_2 analogues of graphene. Angew Chem Int Ed 49(24):4059–4062

28. Teng Y, Zhao H, Zhang Z, Li Z, Xia Q, Zhang Y, Zhao L, Du X, Du Z, Lv P, Swierczek K (2016) MoS_2 nanosheets vertically grown on graphene sheets for lithium-ion battery anodes. ACS Nano 10(9):8526–8535

29. Choi SH, Ko YN, Lee J-K, Kang YC (2015) 3D MoS_2-graphene microspheres consisting of multiple nanospheres with superior sodium ion storage properties. Adv Funct Mater 25(12):1780–1788

30. Yang G, Li X, Wang Y, Li Q, Yan Z, Cui L, Sun S, Qu Y, Wang H (2019) Three-dimensional interconnected network few-layered MoS_2/N, S co-doped graphene as anodes for enhanced reversible lithium and sodium storage. Electrochim Acta 293:47–59

31. Ma L, Ye J, Chen W, Wang J, Liu R, Lee JY (2015) Synthesis of few-layer MoS_2 graphene composites with superior electrochemical lithium-storage performance by an ionic-liquid-mediated hydrothermal route. ChemElectroChem 2(4):538–546

32. Yuan G, Wang G, Wang H, Bai J (2016) Half-cell and full-cell investigations of 3D hierarchical MoS_2/graphene composite on anode performance in lithium-ion batteries. J Alloys Compd 660:62–72

33. Liu X, Shen L, Hu Y (2016) Preparation of TiO_2-graphene composite by a two-step solvothermal method and its adsorption-photocatalysis property. Water Air Soil Pollut 227(5):141

34. Kang J, Balla I, Liu X, Bergeron H, Kim S, Wolverton C, Hersam MC (2018) Selective transfer of rotationally commensurate MoS_2 from an epitaxially grown van der Waals heterostructure. Chem Mater 30(23):8495–8500

35. Li D, Muller MB, Gilje S, Kaner RB, Wallace GG (2008) Processable aqueous dispersions of graphene nanosheets. Nat Nanotechnol 3(2):101–105

36. Lu Z, Liu Q, Xu Z, Zeng H (2015) Probing anisotropic surface properties of molybdenite by direct force measurements. Langmuir 31(42):11409–11418

37. Hu J, Huang B, Zhang C, Wang Z, An Y, Zhou D, Lin H, Leung MKH, Yang S (2017) Engineering stepped edge surface structures of MoS_2 sheet stacks to accelerate the hydrogen evolution reaction. Energy Environ Sci 10(2):593–603

38. Jung Y, Shen J, Liu Y, Woods JM, Sun Y, Cha JJ (2014) Metal seed layer thickness-induced transition from vertical to horizontal growth of MoS_2 and WS_2. Nano Lett 14(12):6842–6849

39. Kong D, Wang H, Cha JJ, Pasta M, Koski KJ, Yao J, Cui Y (2013) Synthesis of MoS_2 and $MoSe_2$ films with vertically aligned layers. Nano Lett 13(3):1341–1347

40. Zhang J, Yang H, Shen G, Cheng P, Zhang J, Guo S (2010) Reduction of graphene oxide via L-ascorbic acid. Chem Commun 46(7):1112–1114

41. Li J, Lin H, Yang Z, Li J (2011) A method for the catalytic reduction of graphene oxide at temperatures below 150°C. Carbon 49(9):3024–3030

42. Ma X, Li N, Liu S, Zhang K, Chi C, Zhao J, Liu X, Li Y (2018) Pyrrolic nitrogen-doped carbon sandwiched monolayer MoS_2 vertically anchored on graphene oxide for high-performance sodium-ion battery anodes. J Solid State Electrochem 22(9):2801–2809

43. Deng Z, Jiang H, Hu Y, Liu Y, Zhang L, Liu H, Li C (2017) 3D ordered macroporous MoS_2@C nanostructure for flexible Li-ion batteries. Adv Mater 29(10):1603020

44. Yu Y, Li C, Liu Y, Su L, Zhang Y, Cao L (2013) Controlled scalable synthesis of uniform, high-quality monolayer and few-layer MoS_2 films. Sci Rep 3(1):1866

45. Kudin KN, Ozbas B, Schniepp HC, Prud'Homme RK, Aksay IA, Car R (2008) Raman spectra of graphite oxide and functionalized graphene sheets. Nano Lett 8(1):36–41

46. Stankovich S, Dikin DA, Piner RD, Kohlhaas KA, Kleinhammes A, Jia Y, Wu Y, Nguyen ST, Ruoff RS (2007) Synthesis of graphene-based nanosheets via chemical reduction of exfoliated graphite oxide. Carbon 45(7):1558–1565

47. Jaber-Ansari L, Puntambekar KP, Kim S, Aykol M, Luo L, Wu J, Myers BD, Iddir H, Russell JT, Saldaña SJ, Kumar R, Thackeray MM, Curtiss LA, Dravid VP, Wolverton C, Hersam MC (2015) Suppressing manganese dissolution from lithium manganese oxide spinel cathodes with single-layer graphene. Adv Energy Mater 5(17):1500646

48. Wang X, Tian J, Cheng X, Na R, Wang D, Shan Z (2018) Chitosan-induced synthesis of hierarchical flower ridge-like MoS_2/N-doped carbon composites with enhanced lithium storage. ACS Appl Mater Interfaces 10(42):35953–35962

49. Wang Y, Ma Z, Chen Y, Zou M, Yousaf M, Yang Y, Yang L, Cao A, Han RP (2016) Controlled synthesis of core-shell carbon@MoS_2 nanotube sponges as high-performance battery electrodes. Adv Mater 28(46):10175–10181